Preconditioned Multigrid Methods for Unsteady Incompressible Flows

C. Liu,* X. Zheng,†,1 and C. H. Sung‡

*Department of Mathematics and Statistics, Louisiana Tech University, Ruston, Louisiana 71272; †Front Range Scientific Computations, Inc., Boulder, Colorado 80304; ‡David Taylor Model Basin, Carderock Division, NSWC, Bethesda, Maryland 20084

A highly efficient numerical approach based on multigrid and preconditioning methods is developed for modeling 3D steady and time-dependent incompressible flows. The k-ω turbulence model is used to estimate the effects of turbulence. The model equations are solved together with the N-S equations in a strongly coupled way, and acceleration techniques like the multigrid method are also used for the turbulence model equations. For unsteady problems, a dual-time stepping procedure is adopted to satisfy the divergence-free constraint and to obtain a time-accurate solution. To improve the performance of this approach for small physical time steps, a modification to residual smoothing parameters is proposed. The numerical algorithm and the turbulence model are validated first by calculating unsteady inviscid flow around an oscillating cylinder, unsteady laminar flow past a circular cylinder, and steady high-Reynolds number turbulent flow over a $6:1$, prolate spheroid. Then the three-dimensional time-dependent turbulent flow over a spheroid when it is undergoing a pitch-up maneuver is calculated and compared with experimental data. ©️ 1998 Academic Press

Key Words: time-dependent flow; incompressible; preconditioning.

1. INTRODUCTION

Simulation of incompressible turbulent flow around naval vehicle models has made considerable progress in recent years [1–5]. While steady flow analysis could give us some insights into the flow physics and is commonly used in the prediction of hydrodynamic performance of underwater vehicles, unsteady flow simulation is of greater significance naturally because most flows are inherently time dependent. In order to enhance the maneuverability of these vehicles, better understanding of the unsteady flow characteristics is in great demand.

---

[1] Corresponding author. Current address: ADINA R & D, Inc., 71 Elton Ave., Watertown, MA 02172.

The major issue in unsteady flow simulation is the computational efficiency, since not only the spatial resolution, but also the temporal resolution is required. Over the last two decades, many methods have been developed to solve the incompressible Reynolds-averaged Navier–Stokes equations. Among those, the pressure-based method and artificial compressibility method are the most successful approaches. The pressure-based methods represented by the SIMPLE-family codes developed by Patankar *et al*. [6] were the dominant approaches in simulation of incompressible flows and compressible subsonic flows during the 1970s and 1980s. There are many industrial codes which use this kind of approach. Some of them have evolved to handle transonic and supersonic flows.

The artificial compressibility methods, proposed by Chorin [7] almost three decades ago, are only getting attention in recent years, partly because of the success of time-stepping schemes in transonic flow calculation. In this approach, an artificial time derivative of pressure is added to the continuity equation, together with a multiplicative variable, β. With this artificial term, the resultant system of equations is symmetric hyperbolic for the inviscid terms. Thus, the system is well posed and efficient numerical methods developed for compressible flows can be used to advance the system in artificial time. Later, Turkel [8] extended this concept and derived more sophisticated preconditioners than those originally proposed by Chorin that render the new equation system well-conditioned for numerical computation. When combined with a multigrid acceleration procedure, this approach has been proven to be particularly effective. Therefore, it is adopted in the present work. The computer code used in this investigation is based on the IFLOW solver developed in the David Taylor Model Basin [1, 4].

For a time-dependent problem, the dual-time stepping technique is used. The physical time derivative terms are treated as source terms. During each physical time step, the system of pseudotemporal equations is solved by advancing in artificial time to reach the pseudo-steady state so that divergence-free constraint on the velocity field is satisfied. Since all the physical terms are treated fully implicitly, there are no stability limitations on the physical time step. All the acceleration techniques developed for time-independent calculations can be used to solve the pseudotemporal equations, such as multigrid, local time stepping, and residual smoothing. This approach was first developed for compressible flows [9–11] and was later adopted for unsteady incompressible flows [12, 13].

Another issue is turbulent modeling. It is noted that most computations of turbulent flows about underwater vehicles employed an algebraic turbulence model. Besides the implementation difficulty of this kind of model in a 3D complex geometry case, its poor performance in the prediction of separation makes it very hard to model the high angle of attack flows. It is widely accepted that the accuracy of modern numerical simulation is largely limited by the accuracy of turbulent modeling. Encouraged by the results reported in [14–18, 5], We use Wilcox's new κ-ω two-equation model in this study.

The present method is first tested by calculating inviscid two-dimensional flow over an oscillating cylinder and unsteady viscous flow past a circular cylinder. In the first case, since the analytic solution is available, strict comparison is made. It was found that our unsteady algorithm is very accurate and very efficient. The mean quantities of second test cases are found in good agreement with experimental data and computational data obtained by other authors. The famous Kármán vortex street phenomenon is clearly captured. Those calculations show that the present method is very efficient and robust, as well as highly accurate. After the turbulence model is tested for three-dimensional turbulent flows over a 6 : 1, pro-late spheroid at various angles of attack, the time-dependent flow over the spheroid when

it is going a 0–30° pitch-up is calculated. Computational results were found in favorable agreement with the available experimental data.

2. GOVERNING EQUATIONS AND THE TURBULENCE MODEL

In this work, the incompressible turbulent flow is simulated by solving the Reynolds-averaged Navier–Stokes equations and turbulence model equations,

$$\frac{\partial u_j}{\partial x_j} = 0 \tag{1}$$

$$\frac{\partial u_i}{\partial t} + \frac{\partial u_i u_j}{\partial x_j} + \frac{1}{\rho}\frac{\partial p}{\partial x_j} + \frac{\partial}{\partial x_j}(\overline{u_i'u_j'}) - \frac{\partial}{\partial x_j}\left[\nu\left(\frac{\partial u_i}{\partial x_j} + \frac{\partial u_j}{\partial x_i}\right)\right] = 0, \quad i = 1, 2, 3, \tag{2}$$

$$\frac{\partial k}{\partial t} + \frac{\partial}{\partial x_j}(u_j k) = \frac{\partial}{\partial x_j}\left[(\nu + \sigma_k \nu_T)\frac{\partial k}{\partial x_j}\right] + \tilde{\tau}_{i,j}\frac{\partial u_i}{\partial x_j} - \beta_k \omega k \tag{3}$$

$$\frac{\partial \omega}{\partial t} + \frac{\partial}{\partial x_j}(u_j \omega) = \frac{\partial}{\partial x_j}\left[(\nu + \sigma_\omega \nu_T)\frac{\partial \omega}{\partial x_j}\right] + (\gamma_\omega \omega/k)\tilde{\tau}_{i,j}\frac{\partial u_i}{\partial x_j} - \beta_\omega \omega^2, \tag{4}$$

where u_j is the velocity, p is the pressure, ρ is the constant density, ν is the molecular kinematic viscosity, k is the turbulent kinetic energy, and ω is the specific dissipation rate. The Reynolds stress tensor $(\overline{u_i'u_j'})$ is modeled by

$$\overline{u_i'u_j'} = \frac{1}{\rho}\hat{\tau}_{i,j} = \tau_{i,j} = \frac{2}{3}\delta_{ij}k - \nu_t\left(\frac{\partial u_i}{\partial x_j} + \frac{\partial u_j}{\partial x_i}\right) \tag{5}$$

$$\nu_t = \gamma_k \frac{k}{\omega}. \tag{6}$$

The closure coefficients are

$$\beta_k = 9/100, \quad \gamma_k = 1, \quad \sigma_k = 1/2, \tag{7}$$

$$\beta_\omega = 3/40, \quad \gamma_\omega = 5/9, \quad \sigma_\omega = 1/2. \tag{8}$$

3. PSEUDO-COMPRESSIBILITY METHODS

The above-described Navier–Stokes equations are solved by using the pseudo-compressibility approach first proposed by Chorin [7] and improved later by Turkel [8] for better condition numbers. Initially this approach was designed to obtain steady-state solutions of the incompressible Navier–Stokes equations by directly coupling the pressure and velocities. Recently, it was also used to solve time-dependent problems [19, 12, 13] by introducing a dual-time stepping technique. Here, the Turkel-type preconditioning method is developed for unsteady moving-grid computation.

In dual-time stepping formulation, the conservative form of preconditioned incompressible N–S equations can be written as

$$P^{-1}\frac{\partial q}{\partial t} + I^1\frac{\partial q}{\partial t^*} + \frac{\partial F}{\partial x} + \frac{\partial G}{\partial y} + \frac{\partial H}{\partial z} = 0, \tag{9}$$

where

$$
q = \begin{pmatrix} p^* = \frac{p}{\rho} \\ u \\ v \\ w \end{pmatrix}, \quad
F = \begin{pmatrix} u - x_{t^*} \\ u(u - x_{t^*}) + p^* - \tau_{xx} \\ v(u - x_{t^*}) - \tau_{xy} \\ w(u - x_{t^*}) - \tau_{xz} \end{pmatrix}
$$

$$
G = \begin{pmatrix} v - y_{t^*} \\ u(v - y_{t^*}) - \tau_{yx} \\ v(v - y_{t^*}) + p^* - \tau_{yy} \\ w(v - y_{t^*}) - \tau_{yx} \end{pmatrix}, \quad
H = \begin{pmatrix} w - z_{t^*} \\ u(w - z_{t^*}) - \tau_{zx} \\ v(w - z_{t^*}) - \tau_{zy} \\ w(w - z_{t^*}) + p^* - \tau_{zz} \end{pmatrix} \tag{10}
$$

$$
\tau_{ij} = (v + v_t)\left(\frac{\partial u_i}{\partial x_j} + \frac{\partial u_j}{\partial x_i}\right) - \frac{2}{3}\delta_{i,j}k,
$$

where t is the pseudo-time, t^* is the physical time, $p^* = p/\rho$, p is the pressure, ρ is the constant density, u, v, and w are the three Cartesian velocity components, $(x_{t^*}, y_{t^*}, z_{t^*})$ are the grid moving velocity. Now the convective velocity is the relative velocity which is equal to the absolute velocity minus the grid moving velocity. v is the molecular viscosity, v_t is the eddy viscosity, I^1 is the unit matrix, except its first element is zero,

$$
I^1 = \begin{bmatrix} 0 & 0 & 0 & 0 \\ 0 & 1 & 0 & 0 \\ 0 & 0 & 1 & 0 \\ 0 & 0 & 0 & 1 \end{bmatrix}, \tag{11}
$$

and P is a preconditioning matrix. Its general form that combines the methods by Chorin, Turkel, and van Leer can be expressed as

$$
P^{-1} = \begin{bmatrix}
(1+\gamma)\beta^{-2} & \gamma\beta^{-2}u & \gamma\beta^{-2}v & \gamma\beta^{-2}w \\
(1+\alpha+\gamma)\beta^{-2}u & 1+\gamma\beta^{-2}u^2 & \gamma\beta^{-2}uv & \gamma\beta^{-2}uw \\
(1+\alpha+\gamma)\beta^{-2}v & \gamma\beta^{-2}vu & 1+\gamma\beta^{-2}v^2 & \gamma\beta^{-2}vw \\
(1+\alpha+\gamma)\beta^{-2}w & \gamma\beta^{-2}wu & \gamma\beta^{-2}wv & 1+\gamma\beta^{-2}w^2
\end{bmatrix}. \tag{12}
$$

In practice, the optimal preconditioning parameters are selected from numerical experiment,

$$
\alpha = 1, \quad \gamma = 0, \quad \beta^2 = \max(|u|^2, \epsilon_\beta), \quad \epsilon_\beta = 0.7. \tag{13}
$$

This approach has been used by Rogers and Kwak [19], Belov, Martinelli, and Jameson [13] in 2D unsteady incompressible flows. Although the simplest preconditioning method of Chorin was used in their studies, very fast convergences were obtained.

The preconditioning matrix P in (12) is only effective for stationary grids. For moving-grid cases, the preconditioning matrix P must be modified to account for the grid-moving velocity. Through a simple analysis of the inviscid governing system, a new preconditioning matrix for the grid-moving case can be derived as

$$
P^{-1} = \begin{bmatrix}
\beta^{-2} & 0 & 0 & 0 \\
\beta^{-2}(2u - x_{t^*}) & 1 & 0 & 0 \\
\beta^{-2}(2v - y_{t^*}) & 0 & 1 & 0 \\
\beta^{-2}(2w - z_{t^*}) & 0 & 0 & 1
\end{bmatrix}, \tag{14}
$$

where

$$\beta^2 = \max((u - x_{t^*})^2 + (v - y_{t^*})^2 + (w - z_{t^*})^2, \epsilon_\beta),$$

$$\epsilon_\beta = 0.7.$$

No preconditioning is needed for convection terms of the turbulence model equations since the wave speeds are already equalized to be the convective velocity, which is also one of the eigenvalues of the preconditioned Navier–Stokes equations.

The more important issue in solving turbulence model equations is the treatment of source terms. The source terms of turbulence model equations are usually dominant and stiff near the wall. A point-implicit technique [5] is used to treat the source terms implicitly. The implicit matrix can be regarded as a preconditioning way to alleviate the stiffness.

4. NUMERICAL METHODS

The above governing equations are solved by using a semi-discrete method, in which the spatial terms and temporal terms are discretized separately.

4.1. *Discretization Scheme*

The flow equations (N–S equations) and the turbulence model equations are discretized by using different schemes due to the totally different characteristics of their solutions.

In incompressible flows usually there is no discontinuity phenomenon such as shock waves. High-resolution schemes, like TVD and eigenvalue-based upwind schemes, are not necessary because those schemes are quite expensive and only make a difference near the shock waves. Therefore, for the flow equations the regular second-order central difference scheme is used. Only fourth-order artificial dissipation terms are added to the system (9). Those terms, in higher order than the numerical scheme, only provide additional dissipation to suppress numerical spurious oscillations when the grid size is not small enough to render the physical viscosity effective. Therefore, they will not contaminate the physical solutions as sometimes the second-order dissipation terms might. Our numerical solutions also show that the fourth-order artificial dissipation terms do not affect the accuracy.

Since the fourth-order artificial terms are very small and there is no significant difference between the eigenvalues after preconditioning, it is not worthwhile to use matrix dissipation. In this work, the maximum spectral radii of matrices *PA, PB, PC* are used instead of the matrices $A = \partial F/\partial q, B = \partial G/\partial q, C = \partial H/\partial q$, respectively. Since the maximum eigenvalue of $|PA|$ is smaller than that of $|A|$, less dissipation is added.

However, for the turbulence model equations a high-order upwind-biased MUSCL scheme [20] is used. The reason for that is the steep gradients existing in the k, ω field, especially for ω. A typical distribution of ω in the direction normal to the wall is that the value of ω changes rapidly from about 10^5 or even higher (depends on the grid resolution) near the wall to the order of 1 outside the boundary layer. It is very hard to construct dissipation terms which will stabilize the computation and avoid introducing excessive dissipation in some regions for a central difference scheme. On the other hand, the high-resolution scheme is designed to deal with such large gradients. The turbulence model equations have a very simple wave structure. Therefore, various orders of upwind schemes can be easily constructed based on the local convective velocities.

The diffusive terms of a Navier–Stokes equation and the turbulence model equations are discretized by a compact central difference scheme with second-order accuracy.

4.2. Time-Stepping Method

After being discretized in space, Eq. (9) can be written as

$$P^{-1}\frac{d}{dt}(V_{i,j,k}q_{i,j,k}) + R_{i,j,k}(q) = 0, \tag{15}$$

where $R_{i,j,k}(q)$ is the total residual,

$$R_{i,j,k} = S_{i,j,k}(q) + I^1 E_{i,j,k}(q) = 0, \tag{16}$$

where $V_{i,j,k}$ is the volume of cell (i, j, k), $S_{i,j,k}(q)$ is the spatial term which includes the convection, diffusion, and dissipation terms, $E_{i,j,k}(q)$ is the real time-dependent term for unsteady flows, which is discretized by using a second-order accurate implicit backwards difference formula:

$$E_{i,j,k}(q) = \left(\frac{1}{2\Delta t^*}\right)[3(V_{i,j,k}q_{i,j,k})^{n+1} - 2(V_{i,j,k}q_{i,j,k})^n + (V_{i,j,k}q_{i,j,k})^{n-1}]. \tag{17}$$

In this work, a five-stage Runge–Kutta-type scheme is used to advance the solution in pseudo-time with the implicit calculation of the unsteady term as shown in (17). Since the pseudo-transient evolution is not of interest, the time stepping scheme can be optimized for faster convergence. Acceleration techniques like multigrid method, local pseudo-time stepping and residual averaging are applied following [21, 22].

The preconditioner and the implicit treatment of the real time-dependent terms are implemented by devising a new updating formula for the Runge–Kutta scheme. For example, in the mth stage of Runge–Kutta scheme at nth pseudo-time step, the updating formula reads

$$P^{-1}\frac{\Delta q^{n,(m)}}{\Delta t^{(m)}} = -\left(R\left(q^{n,(m-1)}\right) + \lambda I^1\left(q^{n,(m)} - q^{n,(m-1)}\right)\right), \tag{18}$$

where

$$\Delta q^{n,(m)} = q^{n,(m)} - q^n, \tag{19}$$

$$\lambda = \frac{3\Delta t^*}{2}, \tag{20}$$

$$\Delta t^{(m)} = K_m \Delta t, \tag{21}$$

where Δt^* is the physical time step, Δt is the local pseudo-time step, and K_m is the Runge–Kutta coefficient of the mth stage. To find the new value $q^{n,(m)}$, an intermediate step is introduced to find the intermediate value $q^{n,(m')}$ which is obtained from

$$P^{-1}\frac{\left(q^{n,(m')} - q^n\right)}{\Delta t^{(m)}} = -R\left(q^{n,(m-1)}\right), \tag{22}$$

as usually done in the normal update without real time-dependent terms.

By subtracting (22) from (18), we have

$$P^{-1} \frac{\left(q^{n,(m)} - q^{n,(m')}\right)}{\Delta t^{(m)}} = -\lambda I^1 \left(q^{n,(m)} - q^{n,(m-1)}\right)$$

which can be rearranged as

$$\Theta^{-1} q^{n,(m)} = P^{-1} q^{n,(m')} + \Delta t^{(m)} \lambda I^1 q^{n,(m-1)}, \tag{23}$$

where

$$\Theta^{-1} = \left\{ P^{-1} + \Delta t^{(m)} \lambda I^1 \right\}. \tag{24}$$

If Turkel's preconditioner is used,

$$P^{-1} = \begin{bmatrix} \beta^{-2} & 0 & 0 & 0 \\ (1+\alpha)\beta^{-2}u & 1 & 0 & 0 \\ (1+\alpha)\beta^{-2}v & 0 & 1 & 0 \\ (1+\alpha)\beta^{-2}w & 0 & 0 & 1 \end{bmatrix}$$

$$= P^{-1}(\alpha, \beta^2), \tag{25}$$

then

$$\Theta^{-1} = \begin{bmatrix} \beta^{-2} & 0 & 0 & 0 \\ (1+\alpha)\beta^{-2}u & 1 + \Delta t^{(m)}\lambda & 0 & 0 \\ (1+\alpha)\beta^{-2}v & 0 & 1 + \Delta t^{(m)}\lambda & 0 \\ (1+\alpha)\beta^{-2}w & 0 & 0 & 1 + \Delta t^{(m)}\lambda \end{bmatrix}$$

$$= \left(1 + \Delta t^{(m)}\lambda\right) P^{-1}\left(\alpha, \beta^2 \left(1 + \Delta t^{(m)}\lambda\right)\right), \tag{26}$$

where $P^{-1}(a, b)$ denotes the matrix with $\alpha = a$, and $\beta^2 = b$ in (25). With the above relations, Eq. (23) can be written as

$$q^{n,(m)} = \Theta P^{-1} q^{n,(m')} + \Theta \Delta t^{(m)} \lambda I^1 q^{n,(m-1)}$$

$$= \frac{1}{\left(1 + \Delta t^{(m)}\lambda\right)} P\left(\alpha, \beta^2 \left(1 + \Delta t^{(m)}\lambda\right)\right) P^{-1}(\alpha, \beta^2) q^{n,(m')}$$

$$+ \frac{\Delta t^{(m)}\lambda}{\left(1 + \Delta t^{(m)}\lambda\right)} P\left(\alpha, \beta^2 \left(1 + \Delta t^{(m)}\lambda\right)\right) I^1 q^{n,(m-1)}$$

$$= \begin{bmatrix} 1 & 0 & 0 & 0 \\ 0 & \frac{1}{(1+\Delta t^{(m)}\lambda)} & 0 & 0 \\ 0 & 0 & \frac{1}{(1+\Delta t^{(m)}\lambda)} & 0 \\ 0 & 0 & 0 & \frac{1}{(1+\Delta t^{(m)}\lambda)} \end{bmatrix} q^{n,(m')}$$

$$+ \frac{\Delta t^{(m)}\lambda}{\left(1 + \Delta t^{(m)}\lambda\right)} \begin{bmatrix} \beta^{-2} & 0 & 0 & 0 \\ 0 & 1 & 0 & 0 \\ 0 & 0 & 1 & 0 \\ 0 & 0 & 0 & 1 \end{bmatrix} q^{n,(m-1)}.$$

For turbulent flow computation, the flow and the turbulence equations are solved as one system. The above-described techniques are applied equally to the turbulence equations as well as to the flow equations.

4.3. *Modification of the Scheme for Small Physical Time Steps*

It is worthwhile to point out, however, when the physical time step is very small (even smaller than the pseudo-time step), the implicit treatment of time-dependent terms will yield very slow convergence. Jameson suggested [9] those terms should be only treated implicitly when the *CFL* number based on physical time step is greater than 200. In this work, we found that this problem can be removed by devising a new residual smoothing parameter formula in which the small physical time step can be accounted for. For instance, the smoothing parameter in ξ direction can be calculated,

$$\epsilon_\xi = \frac{1}{4} \max\left(0, \left(\frac{CFL}{CFL^*} \frac{\lambda_\xi}{(\lambda_\xi + \lambda_\eta + \lambda_\zeta)}\right)^2 - 1\right), \tag{27}$$

where CFL^* is the maximum stable *CFL* number of the basic explicit scheme without smoothing, λ_ξ, λ_η, λ_ζ are the maximum eigenvalues in the ξ, η, ζ directions, respectively.

The efficiency problem can be solved by setting the *CFL* number in the above equation, not the *CFL* number of the pseudo-time step as people usually do, but

$$CFL = \min\left(CFL_{\Delta t}, \frac{1}{4} CFL_{\Delta t^*}\right), \tag{28}$$

where $CFL_{\Delta t}$ is the *CFL* number based on the pseudo-time step Δt, $CFL_{\Delta t^*}$ is the *CFL* number based on the physical time step Δt^*.

By using the formula (28), uniformly fast convergence can be achieved throughout a wide range of physical time steps.

5. BOUNDARY CONDITIONS

The boundary types encountered in this work are classified as solid wall, symmetrical plane, periodical face, singular line, block interface if multiblock is used, and far field. For viscous flow, a nonslip condition is imposed on the solid wall boundary by setting the flow velocity equal to that of the body, and the zero pressure gradient normal to the surface is specified to determine the pressure on the wall. For inviscid flow, the normal velocity component is set to zero; the only contribution to the conservation law for near wall cell is the pressure on the wall, which can be obtained from the normal momentum equation.

Since ghost cells are introduced to store the variable values and derivatives across the boundary, the boundary conditions for symmetrical, periodical, and block interface are easily accomplished by assigning the ghost cell with the values of corresponding cells. Since there is no flux across a singular line, the boundary conditions for a singular line are obtained through extrapolation, combined with partial averaging.

As has been realized by many researchers, the treatment of far field boundary conditions can have a great impact on the convergence of the solution. For unsteady problems, the improper treatment of far field boundary conditions may severely deteriorate convergence in pseudo-time stepping.

In this work, approximate nonreflecting boundary conditions based on a linearized charac-
teristics approach are constructed to improve the convergence rate. The linearized character-
istic problem is solved along the direction normal to the outer boundary of the computational
domain. The program implementation can be summarized as follows.

Let q_n denote the velocity component in the direction $\mathbf{n}$, the outer normal vector of the
far field boundary, and let $\mathbf{q}_T$ indicate the tangential components. The boundary conditions
for far field can be written as

$$p_b = \frac{\lambda_3 p_f - \lambda_4 p_e + \lambda_3 \lambda_4 (q_{n_f} - q_{n_e})}{\lambda_3 - \lambda_4}$$

$$q_{n_b} = \frac{p_e - p_f + \lambda_3 q_{n_e} - \lambda_4 q_{n_f}}{\lambda_3 - \lambda_4}$$

$$(\mathbf{q}_T)_b = \left(1 - \frac{(p_b - p_e)}{\beta^2}\right)(\mathbf{q}_T)_e, \quad \text{if } q_{n_b} > 0,$$

$$(\mathbf{q}_T)_b = \left(1 - \frac{(p_b - p_f)}{\beta^2}\right)(\mathbf{q}_T)_f, \quad \text{if } q_{n_b} \leq 0,$$

where $\lambda_1 = \lambda_2 = (\tilde{q}_n - \tilde{q}_{n_g}), \lambda_3 = -\lambda_4 = \beta$ for the improved Turkel preconditioning
method. $\tilde{q}_n$ and $\tilde{q}_{n_g}$ are averaged normal velocity components of absolute velocity and grid
moving speed, respectively.

6. COMPUTATIONAL RESULTS

Conveniently, unsteady flows can be categorized into three groups: (1) forced, (2) self-
excited, and (3) the combination of both. The flow in the first category is commonly found
in unsteady body motions or boundary movements, such as in submarine flows when un-
dergoing a maneuver, rotor-type flows, and flows with surface-controlling. The second
category refers to the conditions under which the unsteadiness arises from flow separa-
tion and the associated vortex shedding. The flow in the last category is common, but
obviously the least information is available. However, from the point of view of numeri-
cal simulation, if one can deal with the first two categories, there is no fundamental ob-
stacle preventing the last category, even though the physics of such flow is much more
complicated.

In this work, two test cases in the first two categories are carried out. Then we attempt
to calculate the unsteady turbulent flow over a $6:1$, prolate spheroid when it undergoes
pitch-up maneuvering.

6.1. *Oscillating Circular Cylinder*

The first test case considered for unsteady flow is the incompressible inviscid flow over
a sinusoidally oscillating circular cylinder. This test case is in the first category as defined
above. As pointed out by Belov [13], this case is believed to be a severe test for numerical
computations since an analytic solution is available and no physical dissipation is present.
Therefore, it provides a strict test for both artificial dissipation introduced by the numerical
algorithm and accuracy of discretization for the governing equations, as well as for grid
motion.

In this case, the diameter of the cylinder and the frequency of the force oscillation are chosen to be a unit. The coordinate of the cylinder center is set to

$$x_c(t) = a \cdot \sin\left(2\pi t - \frac{1}{2}\pi\right), \tag{29}$$

where the motion amplitude a is equal to 0.1. The fluid velocity at infinity is assumed to be zero, and the pressure at infinity p_∞ is assumed to be a constant of 1. The exact solution for the incompressible inviscid flow over a moving cylinder can be found in [23]. The surface pressure distribution and drag coefficient in this case reduce to

$$p_s(\theta, t, r) = p_\infty + u_c^2(t)\left(2\cos^2(\theta) - \frac{1}{3}\right) + \frac{1}{2}\frac{du_c(t)}{dt}\cos(\theta), \tag{30}$$

$$C_d(t) = 2a\pi^2 \sin\left(2\pi t - \frac{1}{2}\pi\right), \tag{31}$$

where r is the distance to the center of the cylinder, θ is the angle measured clockwise from the direction of the x-axis, and $u_c(t) = dx_c(t)/dt$.

A grid of 64×32 is used in this computation. The physical time step is set to a constant 0.025. Since the analytic solution is available, one can use the exact solution as the initial data to start the unsteady process. However, we found the initial status is not important to the solution of this periodic movement. Instead, a steady solution (by setting time-dependent terms to be zero) is used to start the oscillating process. As shown in Fig. 1, except for the overshooting in the first two steps, the solution quickly converges to the exact solution after a few physical time steps. During each physical time step, less than 50 V(1,0) multigrid cycles or less than 15 W(1,0) multigrid cycles are needed to reduce the residual of continuity equation to below 10^{-4}. The time-evolution of drag coefficient and the body pressure coefficient almost coincide with the analytic solution as shown in Figs. 1 and 2. The computational results fully demonstrate the accuracy and efficiency of our time-dependent solution algorithm.
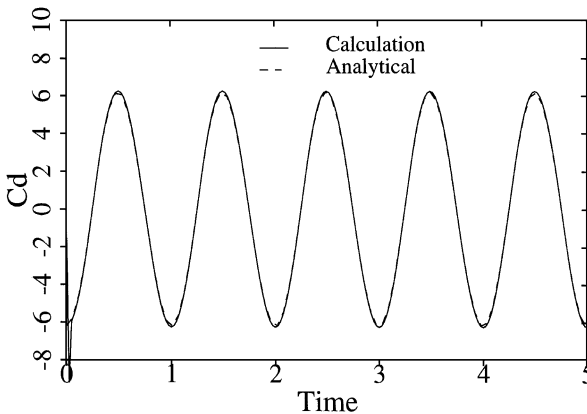
FIG. 1.   Drag coefficient evolution. Inviscid flow over an oscillating cylinder, 64×32 grid.
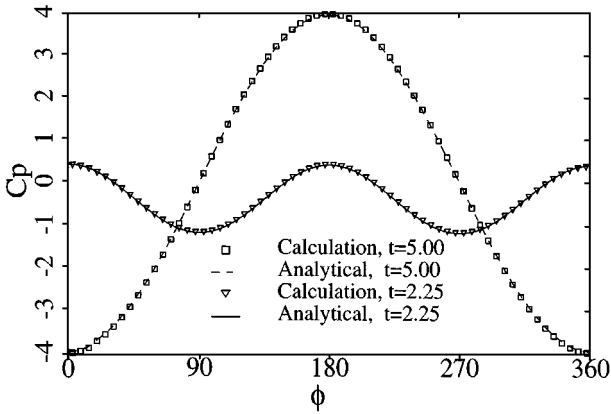
FIG. 2. Pressure coefficient. Inviscid flow over an oscillating cylinder, 64×32 grid.

6.2. *Vortex Shedding from a Circular Cylinder*

The second test case for unsteady flow calculations is the viscous flow passing a circular cylinder, which is the most thoroughly investigated unsteady flow. When the Reynolds number is based on the free-stream velocity and the cylinder diameter is less than 200, the flow will undergo separations but still maintain in laminar stage. The vortices induced by separation are then shed from upper and lower surfaces alternatively and, thus, form the famous Kármán vortex street phenomenon. Three cases with Reynolds number Re = 100, 150, 200 are carried out. The computational results are compared with the numerical results of others and experimental data whenever available.

The physical time step is set to be 0.125. It is about 40–50 steps for each period of vortex shedding, depending on the Reynolds number. The computation starts by rotating the cylinder about its center for a few steps and then stopping, in order to speed up the transition to the limiting cycle and save CPU time. The initial motion affects only the onset time of the asymmetric vortex shedding, but not the characteristics of the limiting cycle itself [13].

Grid refinement study is performed only for the Re = 150 case as shown in Table 1. It can be seen that the results on coarse grids are very close to the results on the very fine grid 256×256. We can expect the solution on the grid of 256×256 to be grid independent. Computation shows that the convergence becomes a little bit slower as the Reynolds number becomes smaller. But generally, about 100 V(1,0) cycles or 20 W(1,0) cycles with seven levels of multigrid can reduce the maximum residual of continuity equation to below 10^{-6}

TABLE 1
Mesh Refinement Results, Re = 150

Grid	4th-order dissipation	S_t	C_d	C_l
64×64	0.01	0.182	1.288 ± 0.018	± 0.432
96×64	0.01	0.182	1.301 ± 0.024	± 0.490
96×96	0.035	0.182	1.305 ± 0.024	± 0.495
96×96	0.00001	0.182	1.308 ± 0.025	± 0.471
96×128	0.01	0.182	1.309 ± 0.025	± 0.486
256×256	0.01	0.182	1.334 ± 0.030	± 0.530
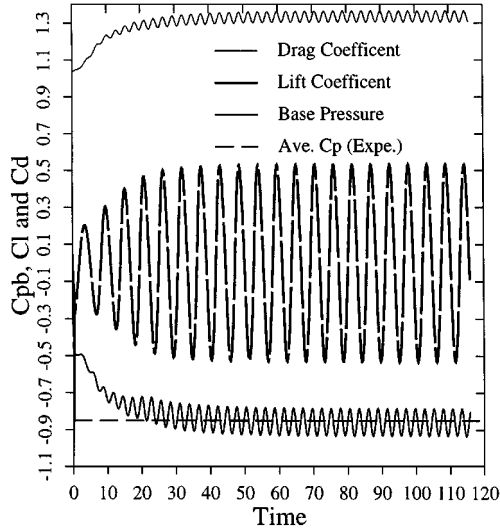
FIG. 3. Pressure, lift, and drag coefficient evolution, Re = 150, grid 256 × 256: Cal. St = 0.182, Cd = 1.33 ± 0.03, Cl = 0 ± 0.53, Exp. St = 0.182(Roshko), 0.183(Williamson), 0.176(Hammache & Gharib).

for each time step. The CPU time of 100 V(1,0) multigrid cycles is found to be less than that of 20 W-cycles on seven levels of grid because the length of vectorization on the coarse grid becomes significantly shorter. The acceleration gains from many iterations on coarse grids in the W-cycle are actually not worthwhile because of the penalty from vectorization, even though the index-link is commonly used in our code to maximize the vectorization length.

Figure 3 shows the time-evolution of drag and lift coefficients and the base-pressure coefficient at 180° from the front stagnation point. The only available experimental data for this case are Strouhal numbers (vortex shedding frequency) and the mean base-pressure coefficient. They are either listed or plotted in Fig. 3. The calculated Strouhal numbers, drag, and lift coefficients are listed under the plot for comparison. We found the numerical results are in excellent agreement with the experimental data.

It is interesting to note in Fig. 3 that the oscillation frequency of the base pressure appears to be twice that of the vortex shedding frequency. But an enlarged examination of the oscillation cycle reveals that the two adjacent cycles are not exactly repeated, as shown in Fig. 4. Therefore, the true frequency of pressure oscillation is still the frequency of vortex shedding.

In Fig. 5, the computed time-evolution of base-pressure coefficient, drag, and lift coefficients are shown for flow with Re = 100. Again, the calculated Strouhal number and base pressure are found in excellent agreement with the experimental data.

More results are shown for the case of Re = 200. First, in Fig. 6, the time-evolution of base-pressure coefficient, drag, and lift coefficients are presented. The computed Strouhal number, mean drag coefficient, and base-pressure coefficient are found in incredibly good agreement with the measured data. The instantaneous streamlines computed at the final stage in our computation is plotted in Fig. 7. Note that they are not particle tracing lines, but just streamlines at one instant moment. Figure 8 shows the contours of vorticities. It basically outlines the Kármán vortex street phenomenon.

Since there have been quite a lot of people who investigated the case of Re = 200, we compile all the results as collected by Belov [13] and Rogers [19] in Table 2. The numerical
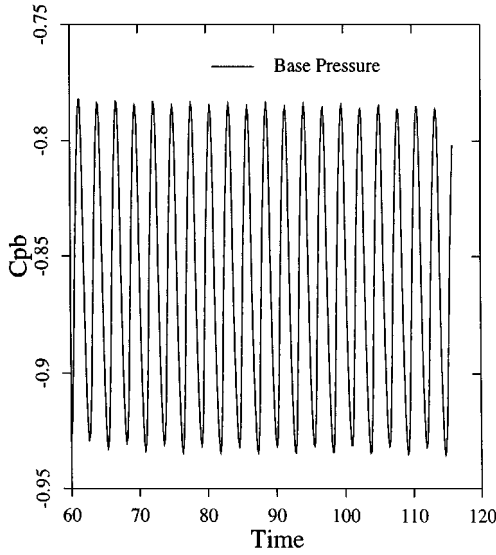
FIG. 4. Base pressure coefficient evolution, Re = 150, grid 256 × 256.

results are listed on the top of the experimental data. By comparing our results with others, it seems the present results are the closest to the experimental data. A plausible explanation for that may be the fact that use of the preconditioning method in our algorithm results in less artificial dissipation required for a stable and efficient calculation.

6.3. *Steady and Unsteady Turbulent Flow*

After testing the present methods for inviscid and laminar flow simulation, we proceed to high Reynolds number turbulent flow over a 6 : 1, prolate spheroid which has been thoroughly investigated by Simpson and his co-workers in their experimental work [24–27]. First, the steady flow with incidence up to 30° was calculated. The numerical results are found in excellent agreement with experimental data. Then the unsteady flow test case described in [27] was calculated and compared with experimental measurements. Although

TABLE 2
Comparison of Results for Unsteady Flow over a Cylinder, Re = 200

| Reference	C_l	C_d	S_t	Base C_p
Present	±0.69	1.31 ± 0.049	0.192	−0.956
Belov *et al.* [13]	±0.64	1.19 ± 0.042	0.193	−0.936
Rogers *et al.* [19]	±0.65	1.23 ± 0.05	0.185	
Miyake *et al.* [13]	±0.67	1.34 ± 0.043	0.196	
Rosenfield *et al.* [19]	±0.69	1.46 ± 0.05	0.211	
Lecointe *et al.* [13]	±0.5	1.58 ± 0.0035	0.194	
Lin *et al.* [13]		1.17		
Henderson [13]			0.197	−1.
Kovaznay (Exp.) [19]			0.19	
Roshko (Exp.) [19]			0.19	
Williamson (Exp.) [13]			0.197	−0.96
Wille (Exp.) [19]		1.3		
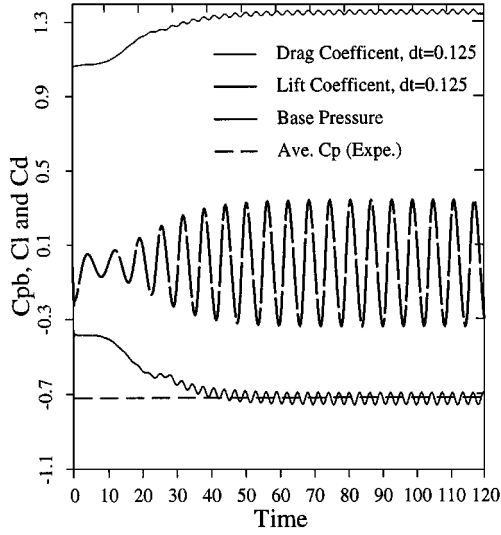
FIG. 5. Pressure, lift, and drag coefficient evolution, Re = 100: Cal. St = 0.165, Cd = 1.350 ± 0.012, Cl = 0 ± 0.339, Exp. St = 0.164(Roshko), 0.166(Williamson), 0.156(Hammache & Gharib).
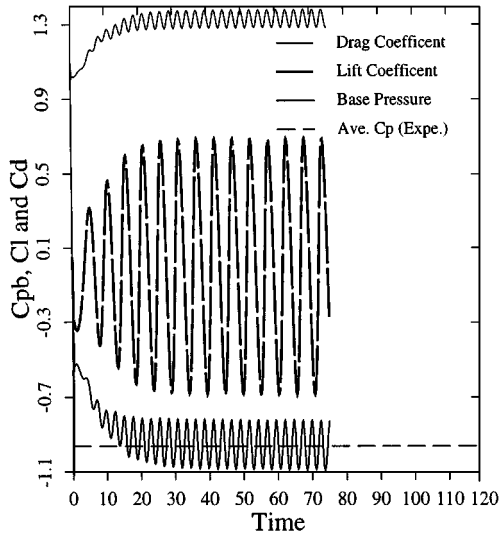
FIG. 6. Pressure, lift, and drag coefficient evolution, Re = 200: Cal. St = 0.192, Cl = 0 ± 0.69, Cd = 1.31 ± 0.049, Exp. St = 0.190(Roshko), Cd = 1.3(Wille), Exp. St = 0.19(Kovasznay).


FIG. 7. Instantaneous streamlines colored by velocity magnitude. Unsteady viscous flow past a circular cylinder. Re = 200, 256 × 256 grid.
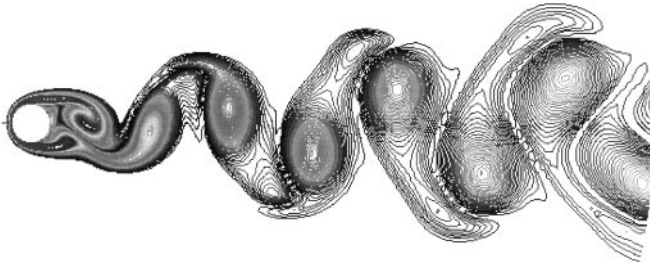
FIG. 8. Vorticity magnitude contours. Unsteady viscous flow past a circular cylinder. Re $= 200$, 256×256 grid.

the idea of simulation of unsteady turbulent flow by using Reynolds averaged Navier–Stokes equation and turbulence model is debatable, it is regarded as the only feasible approach for large scale engineering problems with presently available computer resources.

Since the geometrical model is axisymmetric, only half the domain of flow field is actually simulated. For the steady flow cases, four different sizes of grid, $48 \times 24 \times 32$, $64 \times 32 \times 48$, $96 \times 48 \times 64$, and $128 \times 64 \times 96$ (axial by circumferential and by radial direction), are used in the study to make sure the grid resolution is enough for the flow field and for the solution of turbulence model equations. Figures 9–16 show the results for the case of Reynolds number of 4.2×10^6 and angle of attack of $10°$. The skin friction distribution along the circumferential direction at different axial locations are accurately predicted on the grid of $64 \times 32 \times 48$ as shown in Fig. 9, although an even better prediction is obtained on the finest grid as shown in Fig. 10. As pointed out by Wetzel [27], the wall skin friction minimum qualitatively corresponds to the separation location in spheroid cases. Therefore the accurate prediction of skin friction implies the separation locations are also accurately predicted by k-ω model in this case. The axial, circumferential, and radial velocity component profiles at different axial sections (x/L) and different circumferential locations (ϕ) are plotted against experimental data in Figs. 11–14. It can be found that there is very little difference between the results obtained on the four different grids, and they are almost equally accurate. The same conclusion can be drawn for the surface pressure coefficient distribution as shown in Fig. 15. However, from Fig. 16, it becomes apparent that the mesh resolution of grid $48 \times 24 \times 32$ is not fine enough to predict Reynolds stresses, even though its result is much closer to the experimental data. The over-prediction of Reynolds stress in the outer
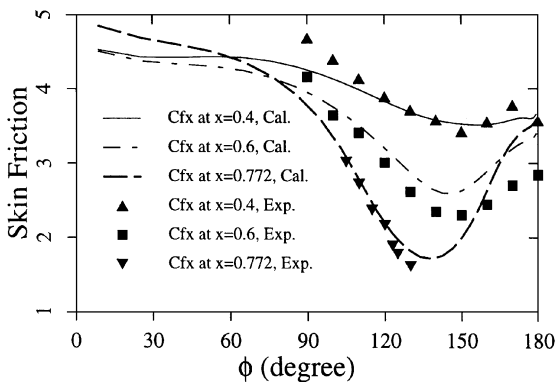
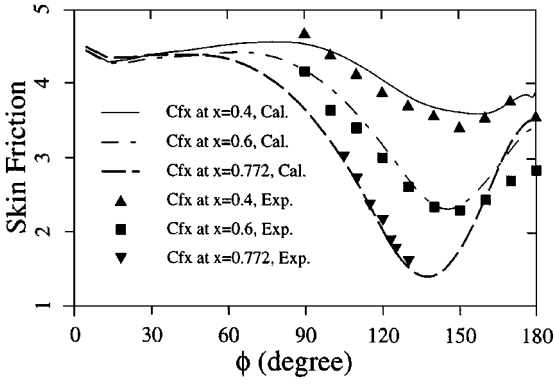**FIG. 9.** Skin coefficients obtained on a grid of $64 \times 32 \times 48$.

FIG. 10. Skin coefficients obtained on grid of $128 \times 64 \times 96$.
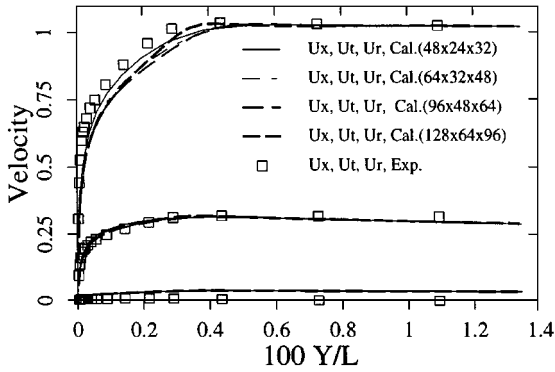

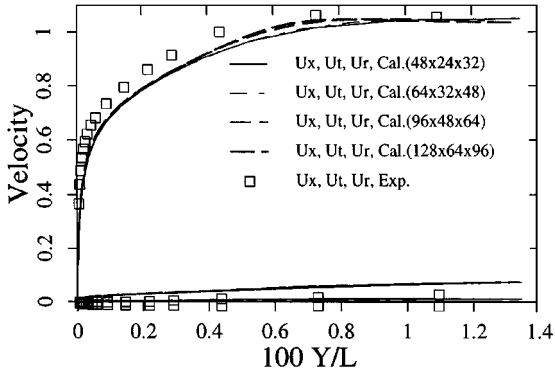**FIG. 11.** Velocity profiles at $x/L = 0.4$, $\phi = 90°$.

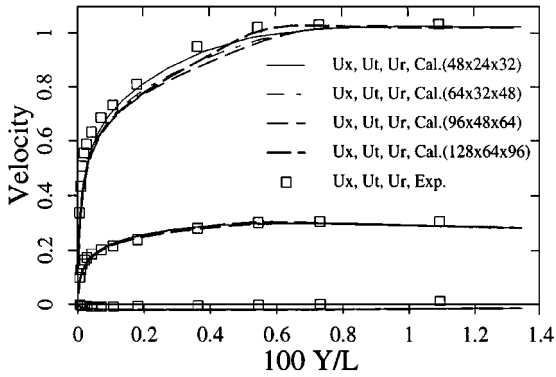**FIG. 12.** Velocity profiles at $x/L = 0.4$, $\phi = 180°$.

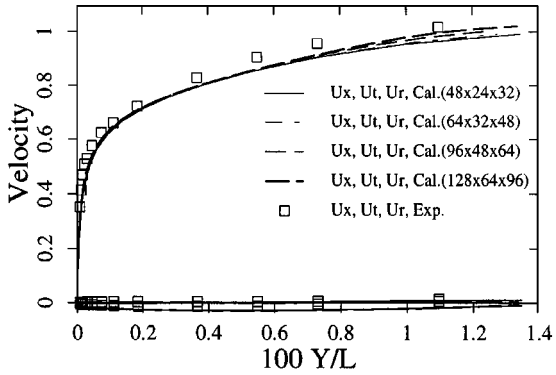**FIG. 13.** Velocity profiles at $x/L = 0.6$, $\phi = 100°$.

FIG. 14. Velocity profiles at $x/L = 0.6$, $\phi = 180°$.

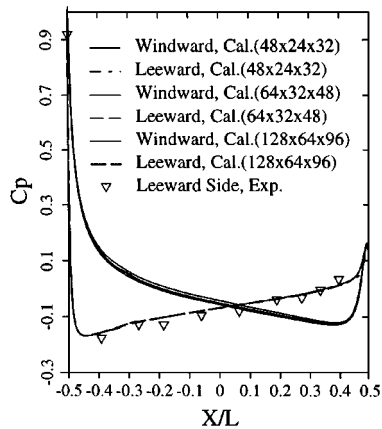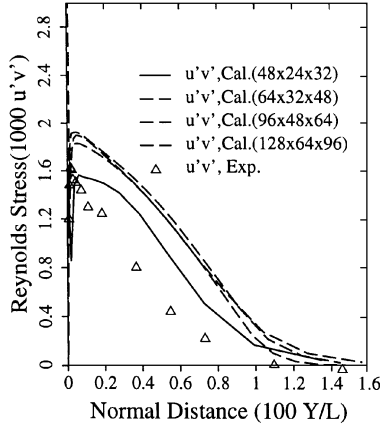**FIG. 15.** Pressure coefficients distribution $Re = 4.2 \times 10^6$, angle of attack $\alpha = 10°$.

FIG. 16. Reynolds stress distribution $Re = 4.2 \times 10^6$, angle of attack $\alpha = 10°$.

boundary layer region is a known problem for the k-ω model. With the results of three finest grids falling so close to each other, we can safely conclude that the grid of $64 \times 32 \times 48$ provides sufficient resolution for engineering calculation in this case.

Figures 17 and 18 show the calculated normal force and pitch moment at different angles of attack and the experimental results. Computational results match the measurements excellently, except in the high angle of attack regime, where the normal force is noticeably underpredicted and the pitch moment is slightly overpredicted. The discrepancy may be caused by the turbulent modeling or may simply be due to asymmetrical vortex shedding at the high angle of attack.

Most calculations are done in 300 multigrid cycles with reducing the residuals by 5 orders of magnitude.

The last test case is the unsteady flow over the same spheroid model when it is doing a pitch-up movement around its geometrical center from 0° to 30° at a constant angular rate of 0.015π.

Only two grids, $48 \times 24 \times 32$ and $64 \times 32 \times 48$, were used in this case because of the heavy CPU time usage required for time-dependent calculation. The total CPU time on a
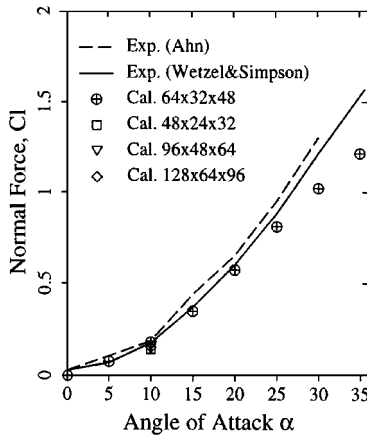

FIG. 17. Normal force vs angle of attack; $6:1$, prolate spheroid, $Re = 4.2 \times 10^6$.
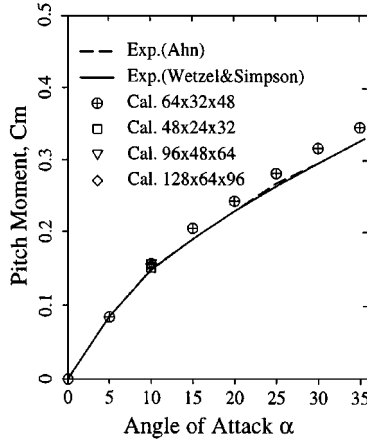
FIG. 18. Pitch moment vs angle of attack; 6 : 1, prolate spheroid, Re $= 4.2 \times 10^6$.

Cray-C90 with use of a single processor is about 4 h if the residual is required down to 10^{-6} at each physical time step on the grid of $64 \times 32 \times 48$. Fortunately, it is not necessary to reduce the residual so low at each time step, and from the calculation results of steady flow, we think the grid of $64 \times 32 \times 48$ is fine enough.

Figures 19 and 20 show the variation of pressure coefficient distribution at two axial sections when the pitch-up motion reaches different angles. Compared with the experimental data, the calculation slightly underpredicts the low and high pressure peaks in the high angle of attack regime. Time evolutions of the body normal force and pitch moment are plotted in Figs. 21 and 22, respectively. Results obtained on two grids and with different physical
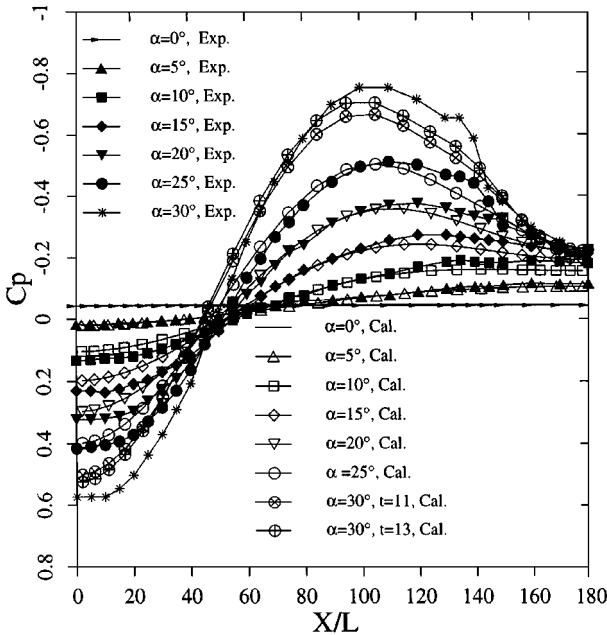

FIG. 19. Pressure distribution at $x = 0.11$. Re $= 4.2 \times 10^6$, unsteady flow during a pitch-up.
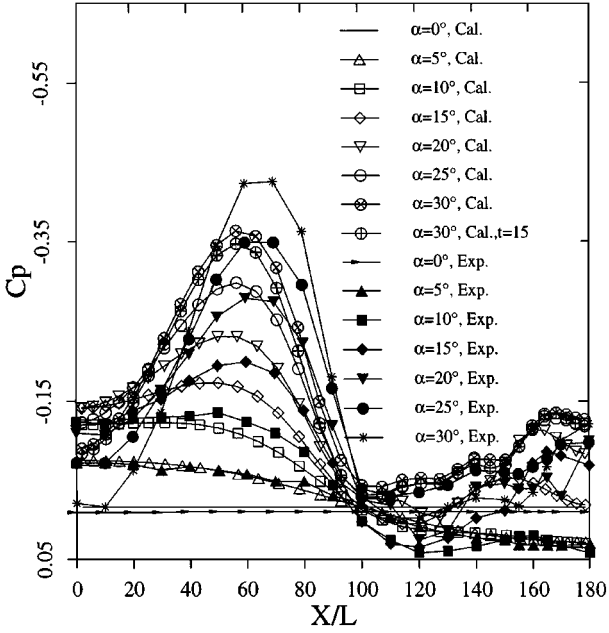
FIG. 20. Pressure distribution at $x = 0.90$. $Re = 4.2 \times 10^6$, unsteady flow during a pitch-up.
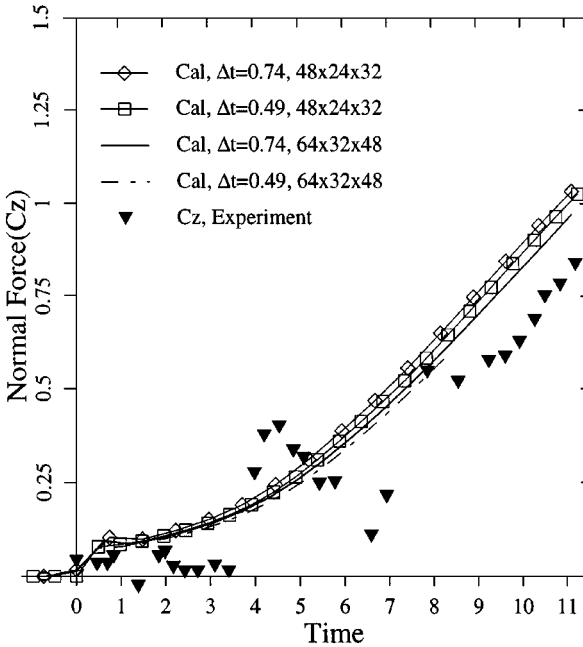

FIG. 21. Time evolution of normal force during a pitch-up; $Re = 4.2 \times 10^6$.
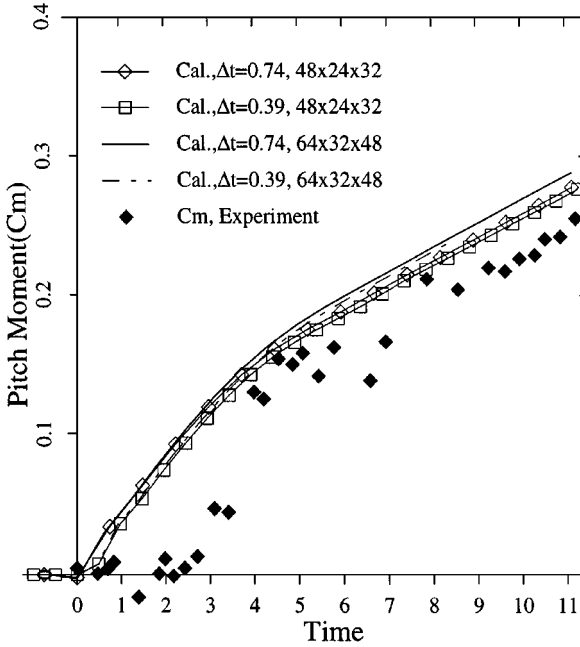
FIG. 22. Time evolution of pitch moment during a pitch-up; $Re = 4.2 \times 10^6$.

time steps are compared with the experimental data. It seems to the authors that more careful work is needed on both numerical and experimental sides. The big oscillation of experimental data may indicate that the designed pitch-up motion is not achieved in actual implementation.

7. CONCLUDING REMARKS

A very efficient and accurate numerical approach based on multigrid and preconditioning methods is developed in this work for predicting three-dimensional steady and time-dependent turbulent flows. The following conclusions are drawn from our computations.

The preconditioning method not only improves computational efficiency, but also numerical accuracy since less artificial dissipation is required for a stable and efficient calculation.

High-order upwind-biased schemes with limiters are a good choice for discretization of turbulence model equations. Because of the simple wave structure of the model equations, the upwind scheme only requires slightly more computational effort than the central difference scheme. It has been found robust and accurate.

The dual-time stepping procedure for time-dependent problems has the advantage that the time step is determined solely by the physical time scale of the problem. The performance of this approach for small physical time steps is greatly improved through a modification to the residual smoothing parameters.

The numerical results are found in excellent agreement with experimental data for 2D unsteady laminar flows and 3D steady turbulent flows. However, the test case of 3D unsteady turbulent flow shows that further investigation is needed from both experimental and numerical sides for more rigorous comparison.

ACKNOWLEDGMENTS

REFERENCES

1. C. H. Sung and M. J. Griffin, Improvement in incompressible turbulent horseshoe vortex juncture flow calculations, *AIAA 91-0022,* in *AIAA 29th Aerospace Sciences Meeting, Reno, NV, January 7–10, 1991.*

2. B. Alessandrini and G. Delhommeau, Simulation of three-dimensional unsteady viscous free surface flow around a ship model, *Int. J. Numer. Methods Fluids* **19**, 321 (1994).

3. C. Sheng, L. Taylor, and D. Whitfield, Multiblock multigrid solution of three-dimensional incompressible turbulent flows about appended submarine configurations, *AIAA 95-0203,* in *33rd Aerospace Sciences Meeting and Exhibit, Reno, NV, January 9–12, 1995.*

4. C. H. Sung, T. C. Fu, M. J. Griffin, and T. T. Huang, Validation of incompressible flow computation of forces and moments on axisymmetric bodies at incidence, *AIAA 95-0528,* in *33rd Aerospace Sciences Meeting and Exhibit, Reno, NV, January 9–12, 1995.*

5. X. Zheng, C. Liao, C. Liu, C. Sung, and T. Huang, Multigrid computation of incompressible flows using two-equation turbulent models, *J. of Fluids Engineering*, Vol. 119, December, 1997. [Also presented as *AIAA 97-0626,* January, 1997]

6. S. A. Patankar and D. B. Spalding, A calculation procedure for heat, mass and momentum transfer in three dimensional parabolic flows, *Int. J. Heat Mass Transfer* **15**, 1787 (1972).

7. A. J. Chorin, A numerical method for solving incompressible viscous flow problem, *J. Comput. Phys.* **2**, 275 (1967).

8. E. Turkel, Preconditioned methods for solving the incompressible and low speed compressible equations, *J. Comput. Phys.* **72**, 277 (1987).

9. A. Jameson, Time dependent calculations using multigrid, with applications to unsteady flows past airfoils and wings, *AIAA 91-1596*, June 1991.

10. F. Liu and S. Ji, Unsteady flow calculations with a multigrid Navier–Stokes method, *AIAA 95-2205*, June 1995.

11. S. Ji and F. Liu, Computation of self-excited oscillation of transonic flow around an airfoil in a channel, *AIAA 96-0063*, January 1996.

12. J. Farmer, L. Martinelli, and A. Jameson, Fast multigrid method for solving incompressible hydrodynamic problems with free surfaces, *AIAA J.* **32**(6), 1175 (1994).

13. A. Belov, L. Martinelli, and A. Jameson, A new implicit algorithm with multigrid for unsteady incompressible flow calculations, *AIAA 95-0049*, January 9–12, 1995.

14. D. C. Wilcox, Reassessment of the scale-determining equation for advanced turbulence models, *AIAA J.* **26**(11), 1299 (1988).

15. D. C. Wilcox, A half century historical review of the k-ω model, *AIAA 91-0615*, 1991.

16. F. R. Menter, Performance of popular turbulence models for attached and separated adverse pressure gradient flows, *AIAA 91-1784*, 1991.

17. F. Liu and X. Zheng, A staggered finite volume scheme for solving cascade flow with a two-equation model of turbulence, *AIAA J.* **32**(8), 1589 (1994).

18. X. Zheng and F. Liu, Staggered upwind method for solving Navier–Stokes and k-ω turbulence model equations, *AIAA J.* **33**(6), 991 (1995).

19. S. E. Rogers and D. Kwak, Upwind differencing scheme for the time-accurate incompressible Navier–Stokes equations, *AIAA J.* **28**(2), 253 (1990).

20. W. K. Anderson, J. L. Thomas, and B. Van Leer, Comparison of finite volume flux vector splittings for the Euler equations, *AIAA J.* **24**(9), 1453 (1986).

21. A. Jameson, W. Schmidt, and E. Turkel, Numerical solutions of Euler equations by finite volume methods using Runge–Kutta time-stepping schemes, *AIAA 81-1259*, June 1981.

22. A. Jameson and T. J. Baker, Solution of the Euler equations for complex configurations, *AIAA 83-1929*, July 1983.

23. L. D. Landou and E. M. Lifshitz, *Fluid Mechanics*, Pergamon, Elmsford, NY, 1987.

24. S. Ahn, *An Experimental Study of Flow over a 6 to 1 Prolate Spheroid at Incidence*, Ph.D. dissertation, Aerospace and Ocean Engineering Department, Virginia Polytechnic Institute and State University, 1992.

25. C. J. Chesnakas, R. L. Simpson, and M. M. Madden, *Three-Dimensional Velocity Measurements on a 6 : 1 Prolate Spheroid at 10° Angle of Attack*, VPI-AOE-202, Department of Aerospace and Ocean Engineering Department, Virginia Polytechnic Institute and State University, 1994.

26. N. T. Hoang, T. G. Wetzel, and R. L. Simpson, Unsteady measurements over a 6 : 1 prolate spheroid undergoing a pitch-up maneuver, *AIAA Paper 94-0197*, January 1994.

27. T. Z. Wetzel and R. L. Simpson, Unsteady three-dimensional cross-flow separation measurements on a prolate spheroid undergoing time-dependent maneuvers, in *21st Symposium on Naval Hydrodynamics, Trondhein, Norway, June 1996.*